Version of Record: https://www.sciencedirect.com/science/article/pii/S0966979521003551
Manuscript_5a33e417fd2ad5d16c460042d5fa4118

Optimization of the microstructure and mechanical properties of electron beam welded high-strength medium-entropy alloy $(NiCoCr)_{94}Al_3Ti_3$

Hanlin Peng[a], Yaoyong Yi[a,*], Weiping Fang[a], Ling Hu[b], Ian Baker[c], Liejun Li[b,*], Bingbing Luo[a]

[a] Guangdong Provincial Key Laboratory of Advanced Welding Technology, China-Ukraine Belt and Road Joint Laboratory on Materials Joining and Advanced Manufacturing, China-Ukraine Institute of Welding, Guangdong Academy of Sciences, Guangzhou 510650, China

[b] School of Mechanical and Automotive Engineering, South China University of Technology, Guangzhou 510640, China

[c] Thayer School of Engineering, Dartmouth College, Hanover, NH 03755, USA

Abstracts: The weldability and effects of subsequent heat treatment on the microstructure and mechanical properties of the medium-entropy alloy (MEA) $(NiCoCr)_{94}Al_3Ti_3$ have been explored using electron beam welding (EBW). It was found that EBW joints consist of a supersaturated f.c.c. matrix with coarse, asymmetric columnar grains (17.7-24 μm). The fraction of twins and $\Sigma 3^n$ CSL boundaries in weld joints was only 10% of that in the base metal, a value which increased to 30% after aging at 800°C. The aging also led to improvements in the hardness, tensile strength, and work hardening rate, a result of the precipitation of a high volume fraction (0.29-0.33) of ultrafine (15-17.4 nm dia.) coherent spherical $L1_2$-structured particles. The contributions of the $L1_2$ nanoparticles and Hall-Petch strengthening to the yield strength were estimated to be 537-573 MPa and 105-123 MPa, respectively. The MEA shows excellent weldability and, after aging, good strength (YS~1098 MPa, UTS~1368 MPa) and elongation to failure (~11%) by ductile fracture.

Keywords: Medium-entropy alloys; Electron beam welding; Microstructure; Mechanical properties; Strengthening mechanisms

1. Introduction

Recently, high-entropy alloys (HEAs) and medium-entropy alloys (MEAs) have attracted considerable attention since they can show excellent fracture toughness [1], good strength and ductility [2, 3], good corrosion resistance [4, 5], and radiation resistance [6, 7]. Numerous strengthening mechanisms have been used to enhance the mechanical properties of MEAs, e.g., Hall-Petch strengthening [8, 9], precipitation strengthening [10-13], interstitial strengthening [14-16], defect strengthening [17], and short-range order strengthening [18]. Among them, $L1_2$ nanoparticles strengthened MEAs and HEAs have a superior combination of strength and ductility at cryogenic temperatures [19], room temperature [20], and ambient high temperature [21, 22]. They show great potential to substitute for Ni-based superalloys, titanium alloys, and high-strength steels. For example, Liu et al. [2, 23, 24] have designed several ultra-strong HEAs with yield strengths higher than 1 GPa and fracture strains larger than 25%. Huang et al. [13] also found $L1_2$ nanoparticle-strengthened CrCoNi-based MEAs have superior strength-ductility combinations, with a yield strength of 792 MPa and fracture strain of 38%. Our previous work [25] found $L1_2$ nanoparticle-strengthened $(NiCoCr)_{94}Al_3Ti_3$ MEAs have a high yield strength of 1203 MPa and a good fracture strain of 24%.

Hence, L1 nanoparticle-strengthened HEAs and MEAs show promise as advanced engineering alloys. Weldability is an important alloy attribute for many structural applications. Thus, to promote the

* Corresponding author.
E-mail address: yiyy@gwi.dg.cn (Y.Y. Yi), liliejun@scut.edu.cn (L.J. Li).

© 2021 published by Elsevier. This manuscript is made available under the Elsevier user license
https://www.elsevier.com/open-access/userlicense/1.0/

industrial application of $L1_2$ nanoparticle-strengthened HEAs and MEAs, it is important to determine their weldability. To date, most research on MEAs has focused on their strengthening mechanisms and phase transformations, while little attention has been focused on their weldability. Kashaev et al. [26, 27], Nam et al. [28, 29], and Wu et al. [30] explored the weldability of f.c.c. CoCrFeNiMn HEAs and found CoCrFeNiMn HEAs have good weldability: welds show no cracking and coarse-grained microstructures forms in the weld joint. Oliveira et al. [31] explored the weldability of CoCrFeNiMn HEA to 316 stainless steel using laser-beam welding, while Sokkalingam et al. [32] studied the weldability of $Al_{0.1}$CoCrFeNi HEA to AISI 304 steel using electron-beam welding. Defect-free dissimilar weld joints were obtained and no brittle intermetallic phases were found, indicating good weldability. Equiatomic single-phase f.c.c. CoCrFeMnNi is currently the most studied HEA, while research on $L1_2$ nanoparticle-strengthened HEAs has rarely been undertaken.

The microstructures of $L1_2$ nanoparticle-strengthened MEAs and Ni-based superalloys are very similar, with distributions of γ' precipitates in a f.c.c. matrix. As is well known, a significant challenge for Ni-based superalloys is their susceptibility to liquation cracking [33, 34], especially for superalloys that have high Al+Ti concentrations. For welding techniques with a high energy input, e.g., electron beam welding (EBW), the necessary vacuum during welding protects against oxidation of active elements but also results in a high vapor pressure, which is a challenge for controlling the chemical composition in alloys containing elements with low melting temperature [35].

In order to explore potential applications of HEAs and MEAs, in this paper we examine the weldability of $L1_2$ nanoparticle-strengthened $(CoCrNi)_{94}Al_3Ti_3$ MEAs. Because of the strong affinity of Al and Ti elements, electron beam welding (EBW) was adopted for $(CoCrNi)_{94}Al_3Ti_3$ because the high-vacuum conditions during EBW can prevent oxidation of the weld joint. The effects of heat treatment on the microstructure and mechanical properties of EBW $(CoCrNi)_{94}Al_3Ti_3$ were also studied.

2. Experimental methods

2.1 Materials fabrication

A new magnetic suspension melting technology was used to cast 110 mm dia. × 90 mm high ingots of $(NiCoCr)_{94}Al_3Ti_3$ from pieces of Ni, Co, Cr, Al, and Ti (purity≥99.7 wt.%). A homogenization heat treatment followed by thermomechanical treatments was undertaken to eliminate tiny cast pores and optimize the microstructure. A schematic of the thermomechanical treatment of the MEA is shown in Fig. 1a. There were fours steps, *viz*., (1) the ingots were homogenized at 1150°C for 4 h; (2) hot rolling at 1150°C to a total thickness reduction of 63.33% was used to eliminate the tiny pores in the ingots; (3) the hot-rolled ingots were reheated to 1150 °C and held for 1 h to release residual stresses; (4) the ingots were cold-rolled to a total thickness reduction of 80%. All the heat treatments were followed by water-quenching.

2.2 Electron beam welding methods

To investigate the effects of heat treatment on the microstructure and mechanical properties of the EBW MEA, aging treatments were conducted both before and after EBW. The heat treatments and EBW details are listed in Table 1. 80 × 20 × 2 mm plates were welded using EBOCAM EK150C-EG150-60BL EBW equipment provided by Steigerwald Strahltechnik GMBH. A schematic of the EBW used for the $(NiCoCr)_{94}Al_3Ti_3$ is shown in Fig. 1b. EBW was performed at an accelerating voltage of 150 kV, a current of 6.5 mA, a welding rate of 600 mm/min under a vacuum of 8×10^{-3} Pa. A light color on the surface of the EBW MEA suggests that the high vacuum condition prevented oxidation despite containing several active elements.

Table 1 Sample codes and corresponding heat treatment and EBW parameters.

Sample Codes	Heat treatment		EBW parameters		Heat treatment	
	Temperature (°C)	Time (h)	Current (m)	Speed (mm/min)	Temperature (°C)	Time (h)
W1	800	4	6.5	600		
W2	800	4	6.5	600	800	4
W3			6.5	600	800	4

2.3 Materials characterization

X-ray diffraction (XRD, Rigaku D/ MAX-2500/PC) was used to analyze the phases present in the MEA, using Mo Kα radiation in the range of 10–42° with a step size of 0.01° and a time per step of 2s. Fig. 1c shows the MEAs used for EBW are single-phase f.c.c. phase. To analyze the weld joints, polished samples were etched using 4% nital for 10 seconds and then observed using a ZEISS Axio Imager M2m Optical Microscopy.

Specimens were also examined in a ZEISS Gemini SEM300 scanning electron microscope (SEM) equipped with an EDAX Hikari electron back-scattered detector (EBSD) detector and operated at an accelerating voltage of 20 keV. Samples for EBSD characterization were electrolytically polished with a solution of 10% $HClO_4$ + 90% alcohol, with a voltage of 16 V and a current of 25 mA at -20°C. TSL OIM analysis 7 software was used to analyze the EBSD data. Fracture surfaces were imaged using second electrons (SE) in a FEI QUANT250 SEM operated at an accelerating voltage of 15 keV. The microstructure of the weld joint was also analyzed using a Talos-F200 (scanning) transmission electron microscope (TEM) equipped with a high angle angular dark field (HAADF) detector and operated at an accelerating voltage of 20 keV. Compositional mapping was performed using energy-dispersive X-ray spectroscopy (EDX) using 4 in-column SDD Super-X detectors.

Vickers hardness measurements were performed across the weld in 0.1 mm steps with a load of 200 g, and a dwell time of 22 s. Nanohardness of the MEA specimens was measured using a Hysitron TI980. A maximum load of 1 mN was used, and four measurements were made for each alloy. Tensile tests were performed on dogbone specimens with a size of 15 mm (guage length) × 2.2 mm (width) × 1.25 mm (thickness) using an Instron 5500 testing machine at an initial strain rate of 5×10^{-4} s^{-1}. Three specimens were tested for each alloy.

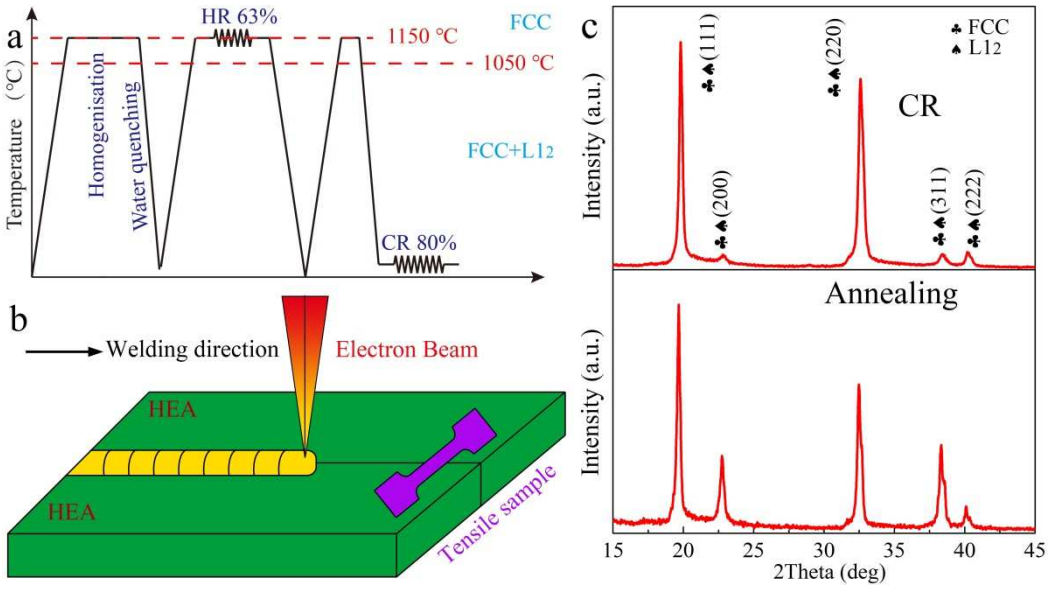

Fig. 1 (a) Schematic of the thermomechanical treatment of the MEA before EBW; (b) Schematic of the EBW procedure; and (c) XRD pattern of the MEAs used for EBW. The top XRD pattern is from the cold-rolled specimen, the lower XRD pattern is from specimen annealed at 800°C for 4h following cold-rolling.

3. Results

3.1 Microstructural analysis

The macrostructure of a cross-sectioned weld joint is shown in Fig. 2, revealing full depth penetration for the EBW W2 specimen. Three distinct zones composed of welding joint, heat-affected zone (HAZ), and base metal (BM) could be observed. The weld joint and BM zone are separated by the weld interface, resulting from a change in microstructure arising from the local heat input during the EBW procedure. The weld center has a columnar-grained microstructure, suggesting the absence of columnar to equiaxed grain transition during solidification, while the microstructure of the HAZ is largely equiaxed grains. The width of the weld joint measured at the top and bottom surface of the weld was 2.68 mm and 0.72 mm, respectively.

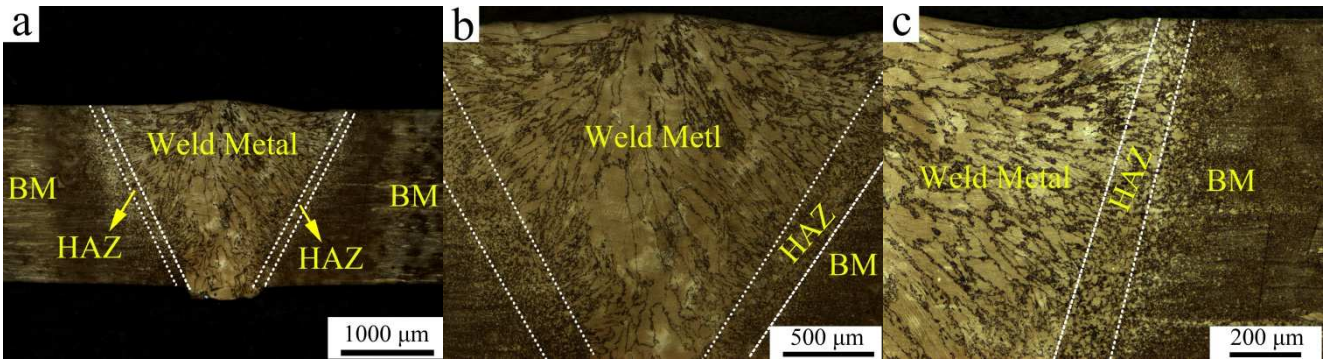

Fig. 2. Optical micrographs of a cross-section of an electron beam weld joint in the W2 specimen: (a) low magnification and (b) high magnification of weld joint; (c) high magnification of weld interface.

EBSD characterization was used to investigate the microstructure of the weld joint and the BM zone. Fig. 3a shows the IPF map of the weld and the HAZ. The weld joint consists of continuous and coarse asymmetric columnar grains, indicating the unidirectional flow of weld pools during the EBW. Similar asymmetric columnar grains were also found in the laser beam-welded 316L stainless steel by Zhu et al. [36]. The inverse pole figure (IPF) reveals the formation of a texture induced by the EBW. The average equivalent diameter of the columnar grains is 24±22 μm, with an average length-width ratio of 2.9±2.0. Fig. 3b shows the kernel average misorientation maps of the weld joint: the average KAM value is 0.375° with a fraction of 61.4%. Similar asymmetric continuous and coarse columnar grains also formed in the weld joint of the EBW W2 (Fig. 4a) and W3 (Fig. 5a) specimens, with an average equivalent diameter of 18.6±17.6 μm and 17.7±17.6 μm, and an average length-width ratio of 2.2±1.0 and 2.5±1.2, respectively.

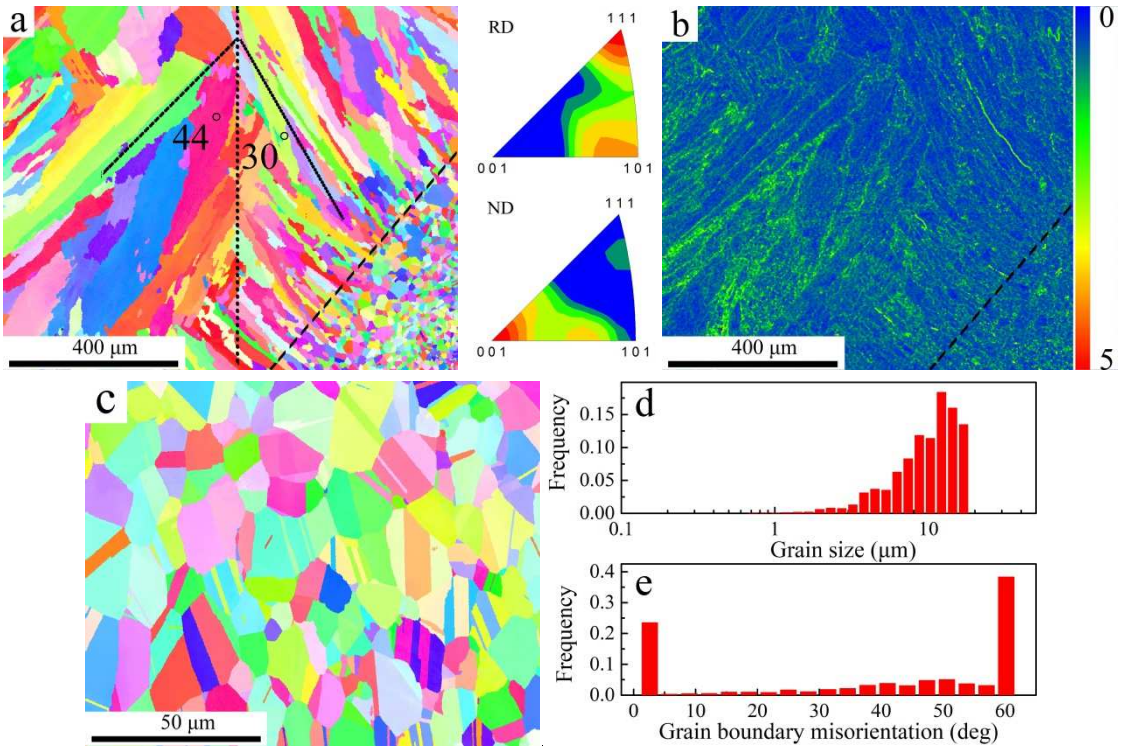

Fig. 3. (a) IPF map and (b) KAM map of the weld joint in the W1 specimen. The IPF is inserted between the IPF map and the KAM map. (c) IPF map, (d) grain size distributions, and (e) grain boundary misorientation angle distribution in the HAZ zone of the W1 specimen.

Average KAM values, which can be used to evaluate the density of geometrically-necessary dislocations (GND), ρ, can be calculated from $\rho=2KAM_{av}/\mu b$ [37], where μ is the step size, and b is the Burgers vector. Comparing the KAM maps (Fig. 3-5), the average KAM for the weld joint in the W2 and W3 specimens is very close to the value for the W1 specimen, but the fraction decreased a bit to 57.4% and 55.8%, respectively. Thus, ρ in the weld joint of three EBW specimens is very close. The results indicate that the annealing treatment following EBW promotes the elimination of residual stress, but the annealing time is not long enough to greatly eliminate the dislocations. Our previous work [25] found the tensile fractured area of annealed nanoparticle-strengthened $(CoCrNi)_{94}Al_3Ti_3$ MEA had an average KAM value of 0.55 (~fraction of 30%). The result indicates that there is some residual stress in the microstructure of the weld joint. As is well known, EBW is a form of fusion welding and inevitably results in residual stresses: the temperature gradient and solidification of the fusion joint both lead to residual stresses [38].

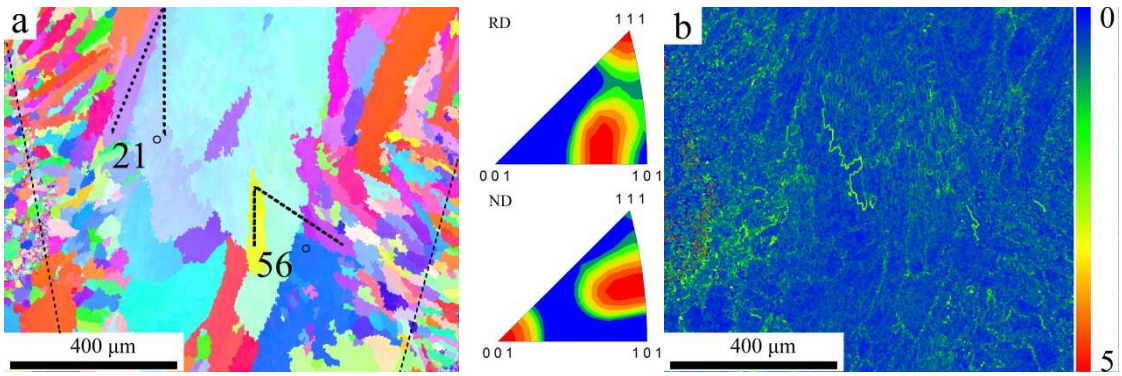

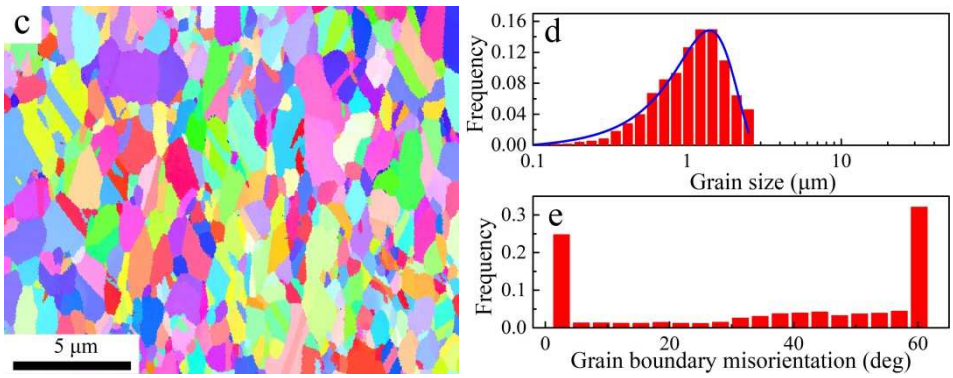

Fig. 4. (a) IPF map and (b) KAM map of the weld joint in the W2 specimen. The IPF is inserted between the IPF map and the KAM map. (c) IPF map, corresponding (d) grain size distributions, and (e) grain boundary misorientation angle distribution of the BM zone in the W2 specimen.

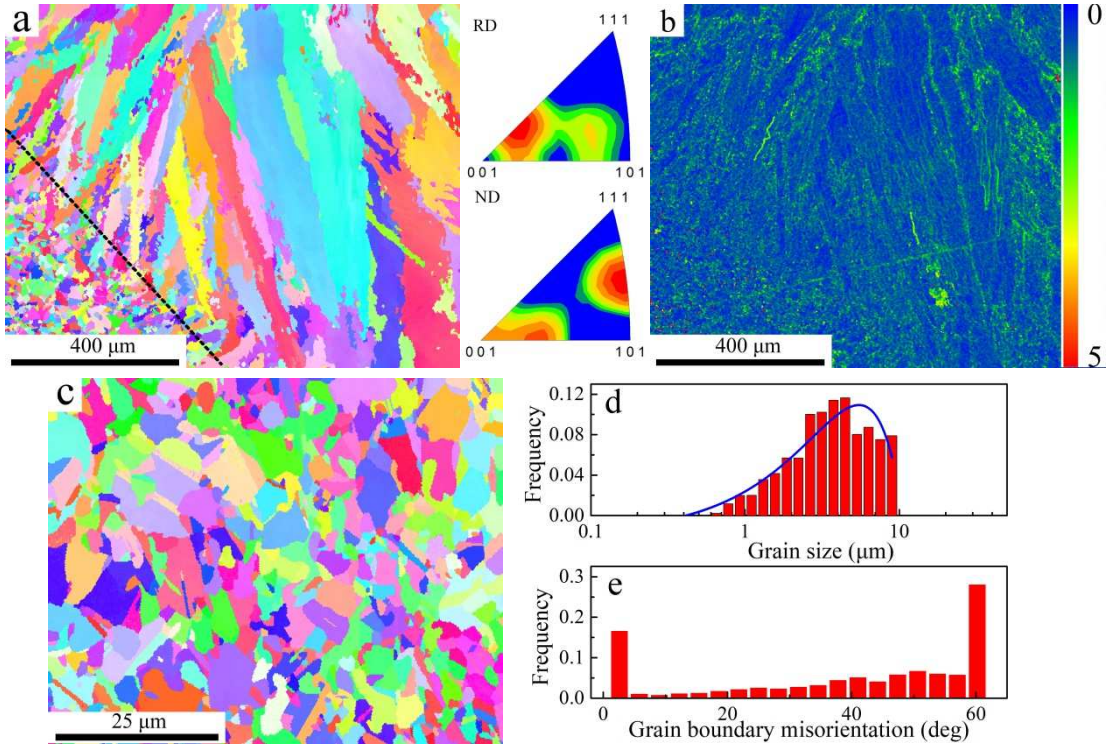

Fig. 5. (a) IPF map and (b) KAM map of the weld joint in the W3 specimen. The IPF is inserted between the IPF map and the KAM map. (c) IPF map, corresponding (d) grain size distributions, and (e) grain boundaries misorientation angle distribution of the BM zone in the W3 specimen.

Table 2 Grain size (GS) and percentages of various special GBs and random grain boundaries (RGB) in the weld joint and the BM/HAZ zone of specimens W1, W2 and W3.

	Weld Joint					BM/HAZ zone				
	GS (μm)	<15°	$\Sigma 3^n$	low ΣGB	RGB	GS (μm)	<15°	$\Sigma 3^n$	low ΣGB	RGB
W1	24±22	5.2	4.3	8.8	81.7	13.4±0.3	3.3	51.5	5.4	39.8
W2	18.6±17.6	9.6	16.5	5.4	68.5	1.4±0.1	4.7	47.2	6.0	42.1
W3	17.7±17.6	9.3	14.8	8.5	67.4	5.5±0.2	3.0	35.5	5.3	56.2

The grain shapes and grain sizes are different in the BM, the HAZ, and the weld joint, as summarized in Table 2. Fig. 3c-3e shows that the HAZ zone in the W1 specimen has an average grain size of 13.4±0.3 μm. The BM zone of the W1 specimen was annealed at 800°C for 4h before EBW, while the BM zone of W3 specimen was annealed at 800°C for 4h following EBW. Therefore, the microstructure of the BM zone for W1 and W3 MEA should be similar. The average grain size in the BM zone of the W2 and W3 specimens are 1.4±0.1 μm (Fig. 4c-4e), and 5.5±0.2 μm (Fig. 5c-5e), respectively, which is lower than that in the weld joint.

Numerous twins could be observed in the IPF map from the BM zone of all three specimens (Fig. 3-5), while twins were rarely observed in the weld joint. Sokkalingam et al. [32] found that the fraction of Coincident Site Lattice (CSL) boundaries in dissimilar weld joints were far lower than that in both the $Al_{0.1}$CoCrFeNi HEA and AISI 304 stainless steel that were welded together. The percentages of different types of grain boundaries (GBs), obtained from the EBSD data, are listed in Table 2. It can be seen that $\Sigma 3^n$ ($\Sigma 3$, $\Sigma 9$, $\Sigma 27$) CSL boundaries in the HAZ zone of the W1 specimen account for 51.5% of GBs, while $\Sigma 3^n$ CSL boundaries in the weld joint are only 4.3% of the GBs. In the weld joints of the W2 and W3 specimens, the $\Sigma 3^n$ CSL boundaries increased to 16.5% and 14.8% of all boundaries. It can be concluded that the percentage of $\Sigma 3^n$ CSL boundaries in the weld joint is far lower than that in the BM/HAZ zone. Also the aging treatment promoted the formation of twins in the weld joint.

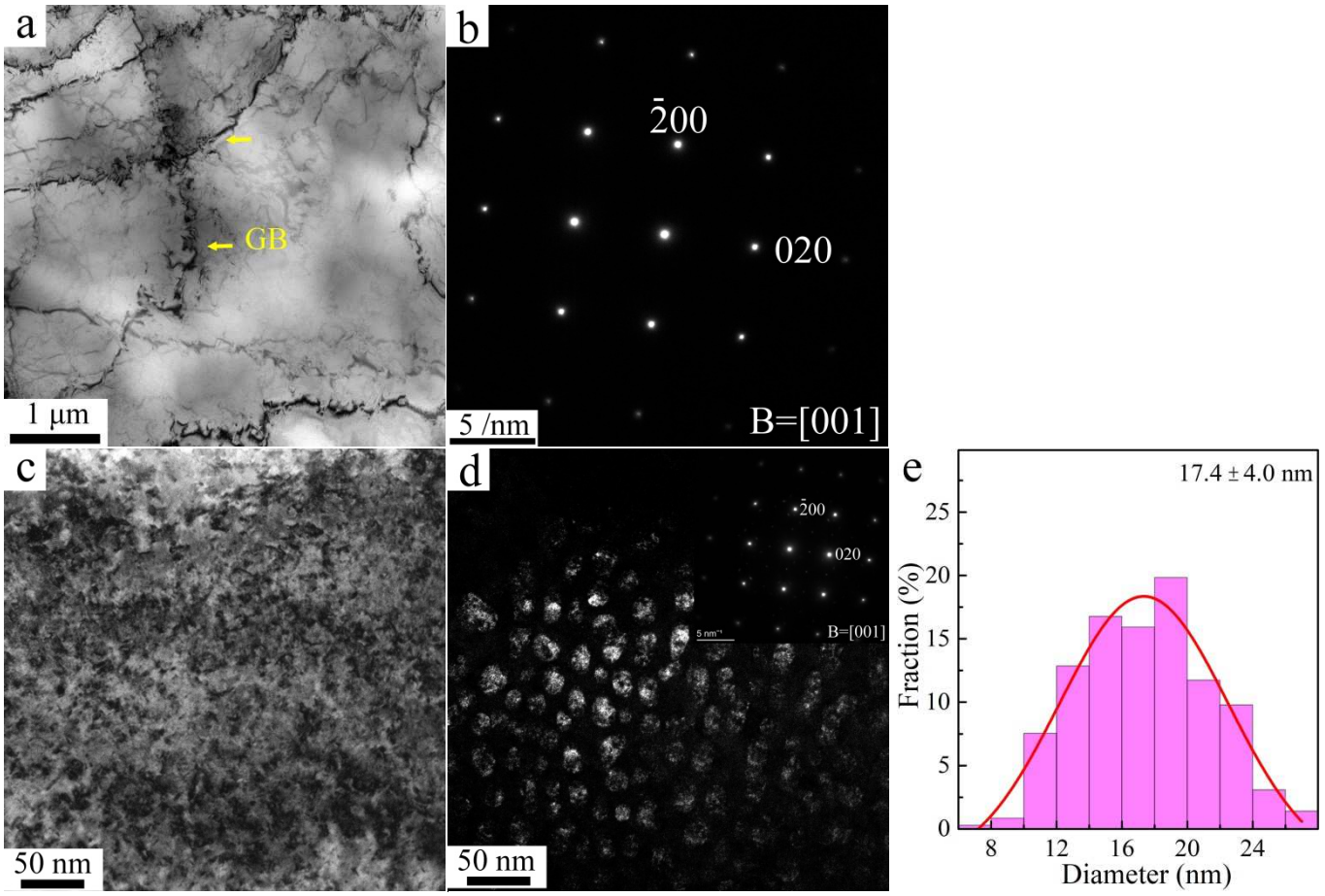

Fig. 6. Weld joint zone of the W1 MEA: (a) bright-field TEM image and (b) SAED pattern viewed at B=[001] confirm that no precipitates are present. Weld joint zone of the W3 MEA: (c) bright-field TEM image showing the $L1_2$ precipitates, (d) DF image showing the morphology and distribution of $L1_2$ nanoparticles using g = [001] of the precipitates with SAED pattern inset; (e) histogram of the diameters of the $L1_2$ precipitates.

The weld joints were further analyzed using a TEM. Fig. 6 shows the weld joint zones of the W1 and W3 specimens. The weld joint zone of the W1 specimen is single f.c.c. phase (Fig. 6a and 6b). In contrast, the weld joint zone of W3 specimen contained a high volume fraction (0.33±0.04) of near-spherical $L1_2$ nanoparticles with an average diameter of 17.4±4.0 nm in a f.c.c. matrix, see Fig. 6c and Fig. 6d. Fig. 7 shows the weld joint zones of the W2 specimens. Fig. 7a shows a HAADF image and corresponding EDX maps showing that the precipitated $L1_2$ phase is enriched with Ni, Ti, and Al and depleted in Cr and Co. Similar elemental distributions have been observed previously [39]. Fig. 7b is a dark field (DF) image, formed using a superlattice diffraction vector g=[001], showing the morphology of the near-spherical $L1_2$ precipitates. The nanoparticles had an average diameter of 15.0±4.0 nm and a volume fraction of 0.29±0.04, as determined using Image-Pro Plus software, see Fig. 7c.

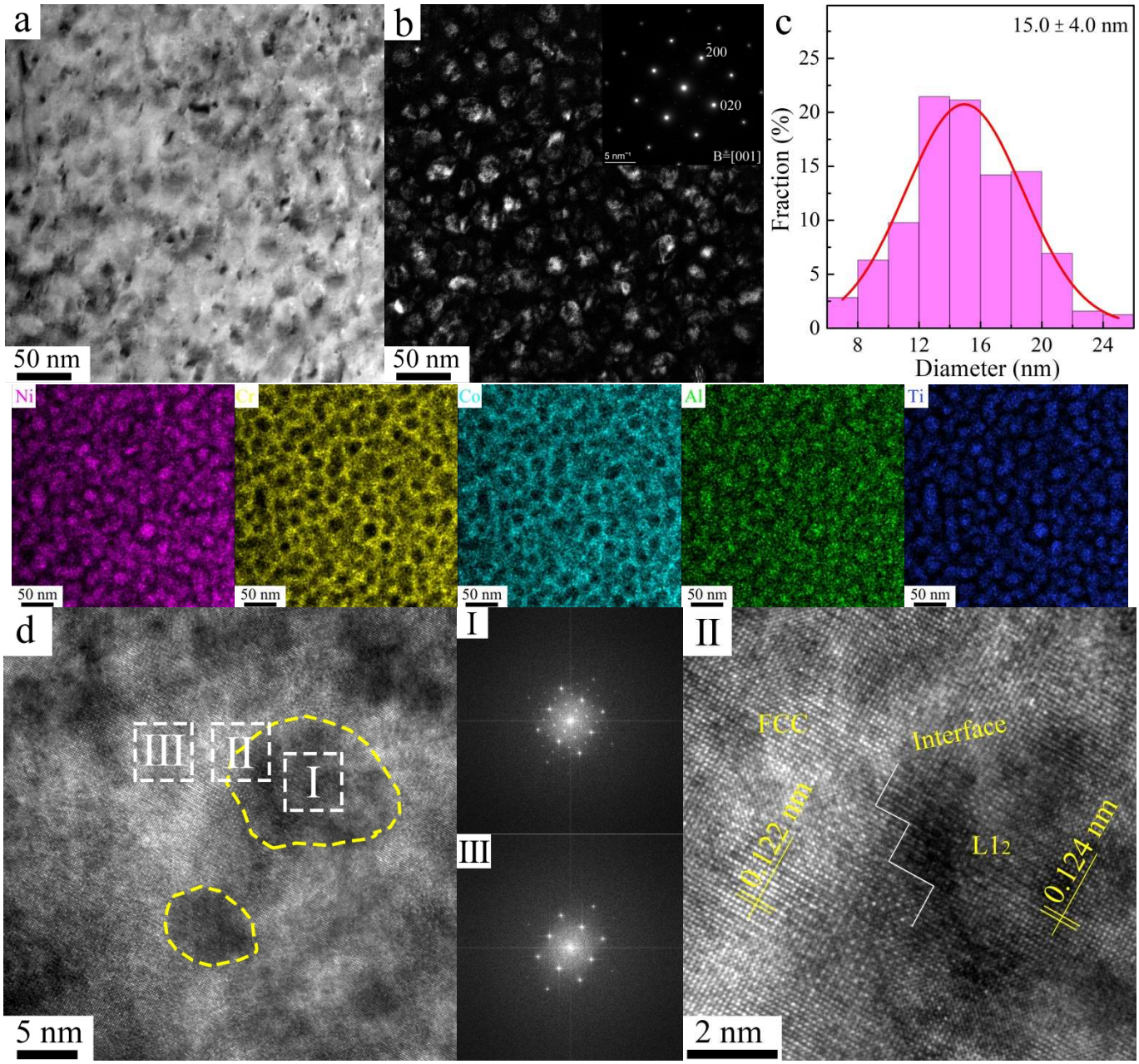

Fig. 7. Weld joint zone of the W2 specimen: (a) HAADF image and corresponding EDX maps showing elemental distribution in the $L1_2$ nanoparticles, (b) DF image showing the morphology and distribution of $L1_2$ nanoparticles obtained using the superlattice diffraction vector g = [001] (SAED pattern is inset); (c)

histogram of the diameters of the $L1_2$ precipitates; (d) HRTEM image and IFFT image of the region marked II in (d) indicating that the $L1_2$ phase is coherent with f.c.c. matrix. The corresponding FFT patterns from the region marked III in (d) indicate single f.c.c. phase, and the region marked I in (d) indicating the presence of $L1_2$ precipitates.

Fig. 7d shows a HRTEM image of the interphase between the f.c.c. matrix and the $L1_2$ precipitates. The f.c.c. matrix, interface, and $L1_2$ particles are marked regions III, II, and I. Utilizing a fast Fourier transform (FFT) and an inverse fast Fourier transform (IFFT), the HRTEM of the interface between the f.c.c. matrix and the $L1_2$ nanoparticles located in region II shows approximate interplanar spacings of 0.122 nm and 0.124 nm, respectively. The coherency of the f.c.c. matrix and the $L1_2$ phase can be estimated using $\delta=2(\alpha_{L12}-\alpha_{FCC})/(\alpha_{L12}+\alpha_{FCC})$, where δ is the lattice misfit, and α_{L12} and α_{FCC} are the lattice parameters of $L1_2$ phase and f.c.c. phase, respectively. A misfit of ~1.6% was obtained based on the HRTEM image.

3.2 Mechanical properties

Fig. 8 shows the Vickers hardness as a function of distance across various welds. Because the EBW joints have a cone shape, the hardness at the top, middle, and bottom of the weld was measured. The hardness of the heat-affected zone (HAZ) and based metal (BM) zone is higher than those of the weld joint for specimen W1. This is because the microstructure of the BM zone consists of $L1_2$ nanoparticles in the f.c.c. matrix, a result of the aging treatment before the EBW. In contrast, the rapid cooling from the melt lead to a supersaturated precipitate-free f.c.c. matrix in the weld joint, as confirmed by the TEM observations (Fig. 6a-6b). The hardness of the BM zone (492, Fig. 8a) is almost twice the value of the weld joint zone (290, Fig. 8a). The widths of the weld joint at the top and bottom was inferred to be 2.79 mm and 1.59 mm, respectively, based on hardness measurements, which are close to the values obtained from optical microscopy (2.68 mm and 0.72 mm, respectively) in Fig. 2. The hardness variations in W2 and W3 specimens are shown in Fig. 8b and Fig. 8c, respectively. The BM and weld joint zone exhibit average hardnesses of 497 and 431, respectively, for the W2 specimen, and average hardnesses of 509 and 422 for the W3 specimen, respectively. Both W2 and W3 specimens were subject to aging treatment following the EBW and Vickers hardness of the weld joint was found to increase by 141 and 132, respectively. This is because the aging treatment after EBW leads to precipitation of nano-sized $L1_2$ phase.

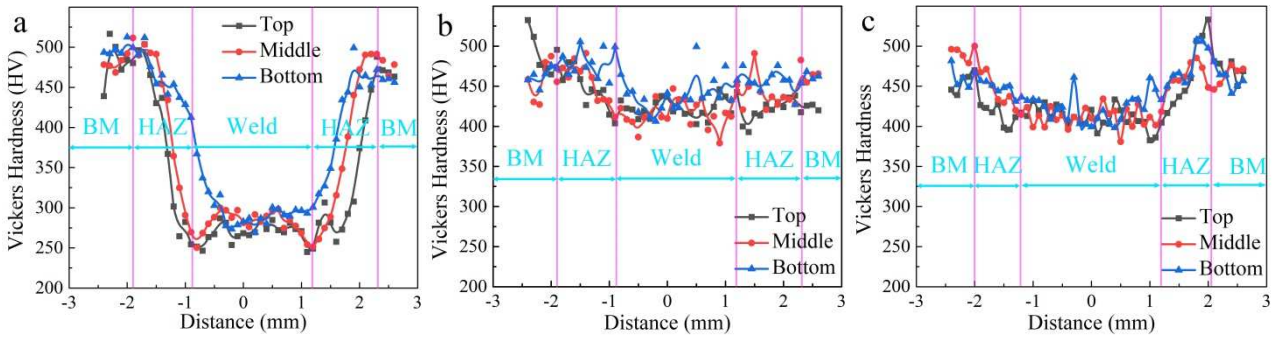

Fig. 8. Vickers hardness as a function of distance across welds for specimens (a) W1, (b) W2, and (c) W3.

Fig. 9a shows typical engineering tensile stress-strain curves at room temperature for the three EBW MEAs. A yield strength (YS) of 615±35 MPa, ultimate tensile strength (UTS) of 872±22 MPa, and a fracture strain of 9.7±0.1% were obtained for the W1 specimens. By comparison, the W2 specimens showed a YS of 1098±25 MPa, a UTS of 1368±19 MPa, and a fracture strain of 11±0.4%, while the W3 specimens exhibited a YS of 1044±26 MPa, an ultimate strength of 1288±14 MPa, and a fracture strain of 7.9±0.1%. Note that the W2 and W3 specimens had similar YS and UTS values. The tensile fracture of all

three samples occurs at the location of the weld joint, indicating that the weld joint has lower strength than the BM zone. Our previous work [25] found that the hot rolled and cold rolled (step 1-4 in Materials fabrication) MEA following annealing at 800°C for 4h has a high YS of 1203 MPa, UTS 1577 MPa, and a fracture strain of 24%. Although the aging treatment following EBW leads to a dramatic increase in hardness (132-141) and tensile strength (>400 MPa in YS), both the tensile strength and fracture strain of weld joint are lower than that of the as-annealed MEA [25]. The YS and UTS of the weld joint reached 87-91% and 82-87% of those of the as-annealed materials, while the fracture strain of the weld joint was only 33-46% of that of the as-annealed materials. This is because the precipitation strengthening from $L1_2$ nanoparticles to YS and UTS is higher than the Hall-Petch strengthening, as analyzed later. In addition, the coarse columnar-grains in the weld joint leads to inferior ductility compared to ultrafine equiaxed grained microstructure, as reported previously [25].

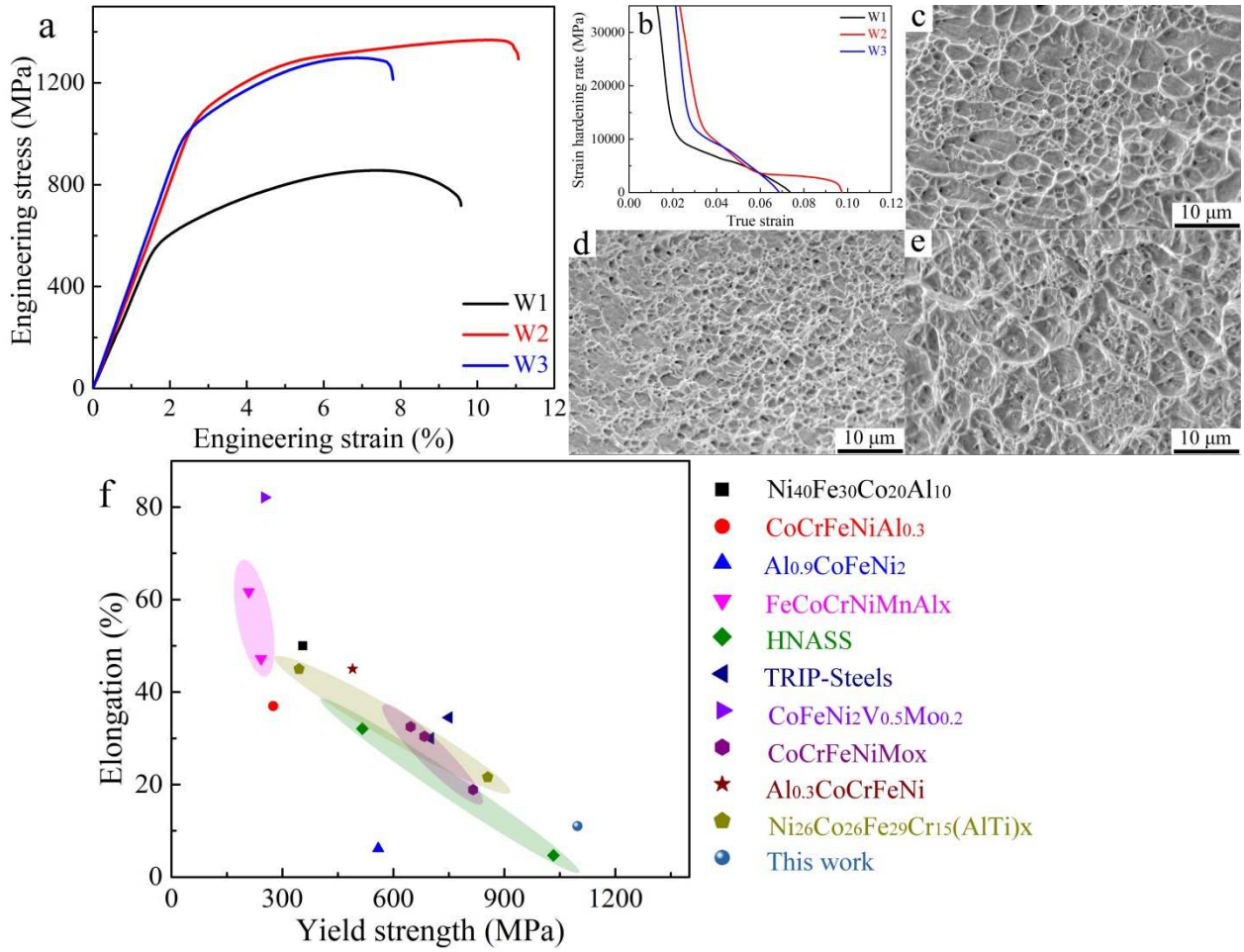

Fig. 9. (a) Tensile engineering stress-strain curves; (b) work hardening rate versus true strain; SE images of the fracture surfaces of (c) W1, (d) W2, and (e) W3 MEA after tensile testing; (f) comparison of the mechanical properties of the EBW MEA with other selected HEAs [20, 40-43] and high strength steels [44, 45].

The work hardening rate, WHR, plotted as a function of true strain is shown for all three EBW samples in Fig. 9b. The WHR decreased with increasing strain. The W2 specimen showed the highest WHR, while W1 specimen had the smallest WHR at the same true strain. For the W2 specimen, the WHR decreased rapidly up to 6% true strain, and then decreased slowly with further increases in strain. Note that the initial WHR at 6% true strain, the WHR of the W2 specimen shows a value of 3621 MPa, which is nearly 2000 MPa higher than that of the ultrafine-grained steels [46] and B2 phase-strengthened HEAs

[47]. This high initial WHR results from $L1_2$ precipitates exerting strong impediments to dislocation movements. Wang et al. [48] found similar behavior and proposed that the obstruction of dislocation movement by grain boundaries and precipitates resulted in the formation of localized high densities of dislocations and further caused unstable deformation at large strains. This may account for the trends in the WHR curves.

All the tensile fractures occurred at the location of the weld joint, and dimples could be observed on the fracture surface, which suggests a ductile fracture mechanism for all the three specimens, see Fig. 9(c-e). Kashaev et al. [26] found that the tensile properties of as-sintered and laser-beam-welded CoCrFeNiMn HEA were almost identical, while the ductility of the weld joint was slightly lower than that of the as-sintered alloy. The latter result and the results in this study indicate that the formation of coarse columnar grains in the weld joint leads to a decrease in ductility. Fig. 9f shows the mechanical properties of the EBW W2 specimen in comparison with both HEAs and high-strength steels (HSSs). It is evident that the EBW MEA has a good combination of strength and ductility at room temperature, making it possible to be used in structural applications. All the results suggest excellent weldability of the studied $(NiCoCr)_{94}Al_3Ti_3$ MEAs.

3.3 Nanoindentation analysis

As discussed above, the BM zone and weld joint have different grain sizes, grain shapes, and phase compositions. Hence, nanoindentation was used to evaluate the difference in nanomechanical properties between the BM zone and weld joint. The weld joint in W1 specimen has an average nanohardness of 5.7±0.9 GPa, which is lower than the 7.4±0.5 GPa of the BM zone. While for the W2 and W3 specimens, the nanohardness of the weld joint and BM zone are very similar, which is similar to the results for the Vickers hardness. The nanohardnesses of the weld joint in W2 and W3 specimens were 7.2±1.0 GPa and 6.3±0.5 GPa, respectively. Similarly, the BM zone in W2 and W3 specimens had average nanohardnesses of 6.3±0.5 GPa and 6.4±0.5 GPa, respectively. The nanohardness and Vickers hardness evolution indicate that the aging treatment following EBW leads to the dramatic strengthening of the weld joint but a slight weakening of the BM zone.

In addition, obvious pop-in behaviors were observed in the weld joint zone, while pop-in points were relatively less in the BM zone. The elastic-plastic behaviors before the first pop-in event can be investigated using the Hertzian elastic contact solution model, which is described by [49]:

$$\mathrm{P} = \frac{4}{3} E_r R_i^{1/2} h^{3/2} \tag{1}$$

and

$$\frac{1}{E_r} = \frac{1-v_i^2}{E_i} + \frac{1-v_s^2}{E_s} \tag{2}$$

where P is the applied load, Ri is the radius of the indenter, h is the indentation depth, Er is the effective indentation modulus, E is the Young's modulus, v is Poisson's ratio, and the subscripts i and s represent the indenter and specimen, respectively. The dashed line in Fig. 10 is the Hertzian solution calculated from Eq. (1). Given a tip radius of 200 nm, the Young's modulus and Poisson's ratio for the indenter and the specimen are 1140 GPa, 0.07 [50] and 214.79 GPa, 0.28 [18], respectively. Both P–h curves deviate from the Hertzian solution at the first pop-in. The maximum shear stress τ_{max} for the elastic regime is given by [50]

$$\tau_{max} = \frac{0.31}{\pi} \times \left(\frac{6PE_r^2}{R_i^2}\right)^{1/3} \tag{3}$$

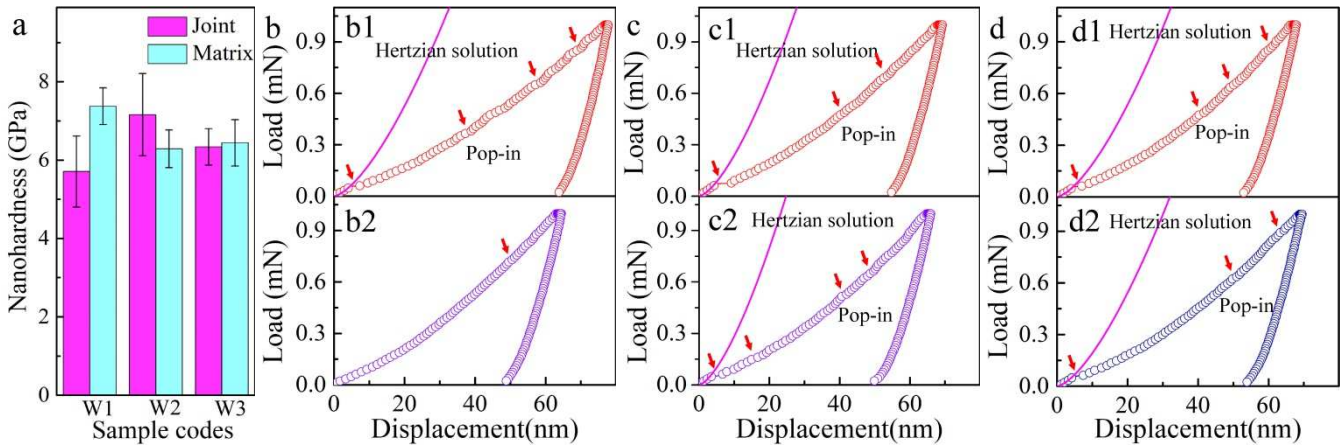

Fig. 10. (a) Nanohardness of the BM and weld joint in various MEAs. Corresponding P-h curves of the indentations for (b) W1, (c) W2, and (d) W3. b1, c2, d3 are indentations on the weld joint, b2, c2, and d2 are indentations on the BM zone. The dashed line is the Hertzian solution and arrows mark the pop-in points.

Based on the P–h curves, the first pop-in loads for the weld joints in the W1, W2 and W3 specimens are 58±15 μN, 58±18 μN, and 63±19 μN, respectively. Based on Eq.(3), the maximum shear stresses for the weld joint in the W1, W2, and W3 specimens are 6.8 GPa, 6.8 GPa, and 7.0 GPa, respectively. The maximum shear stresses for the BM zone in W1, W2, and W3 specimens are 9.1 GPa, 7.0 GPa, and 7.4 GPa, respectively. The maximum shear stresses for both the weld joint and the BM zone are very close to the theoretical strength of 8.0 GPa (10% of the shear modulus), given that the shear modulus G=80 GPa for the MEA [51].

4 Discussion

As discussed above, the Vickers hardness, nanomechanical properties, and mechanical properties of the weld joint of both W2 and W3 specimens are improved after the aging treatment following EBW. This can be explained by considering the calculated phase fractions as a function of temperature, as shown in Fig. 11. The calculated solution temperature of the $L1_2$ phase is around 1080°C, meaning that the aging treatment at 800°C will promote precipitation of the $L1_2$ phase. From Table 1, the W1 specimen is subject to aging treatment before the EBW, which leads to a microstructure consisting of $L1_2$ precipitates in the f.c.c. matrix in the BM zone. However, the high cooling rate in the weld joint zone results in a single-phase supersaturated microstructure. As a result, the nanomechanical properties and tensile strength of the BM zone are higher than those of the weld joint zone. Both W2 and W3 specimens are subject to aging treatment after the EBW, which leads to the precipitation of the $L1_2$ phase in the weld joint zone. An increase in hardness and mechanical properties of the weld joint zone was obtained, which is a little lower than in the BM zone.

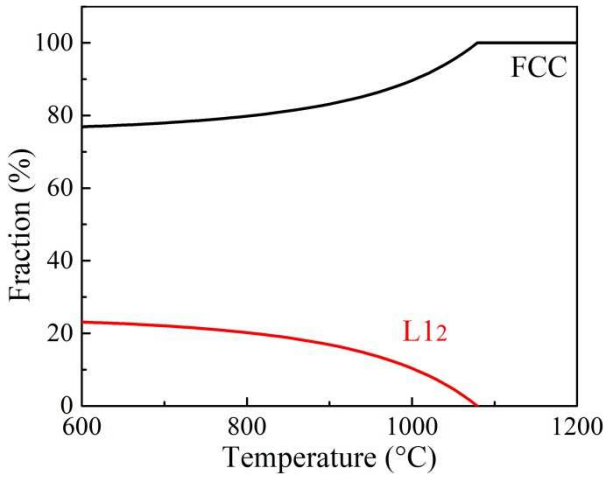

Fig. 11. Phase fraction as a function of temperature for $(NiCoCr)_{94}Al_3Ti_3$ HEA calculated using Jmatpro.

A high volume fraction (0.33) of coherent $L1_2$ nanoparticles (17.4 nm) in the W3 specimen and a high volume fraction (0.29) of coherent $L1_2$ nanoparticles (15.0 nm) in the W2 specimen are present in the weld joint zone after aging, which enhance the nanomechanical properties and tensile strength. The yield strength σ_y in alloys can be described by strengthening from four mechanisms [45], i.e.

$$\sigma_y = \sigma_i + \sigma_{gb} + \sigma_{ss} + \sigma_p \quad (4)$$

where the σ_i is the lattice friction, σ_{gb} is the grain boundary strengthening, σ_{ss} is the solid solution strengthening, and σ_p is the precipitation strengthening. From previous work [20], the contribution from grain boundary strengthening can be estimated from

$$\sigma_{gb} = K_y \times \frac{1}{\sqrt{d}} \quad (5)$$

in which *Ky* is the Hall-Petch strengthening coefficient and d is the average grain size [45, 52]. Liu et al. [53] obtained a *Ky* of 516 MPa×μm$^{1/2}$ for the $Ni_{32.8}Fe_{21.9}Co_{21.9}Cr_{10.9}Al_{7.5}Ti_5$ HEA and Yoshida et al. [52] reported CoCrNi MEA had a *Ky* of 218 MPa×μm$^{1/2}$. Considering the addition of Al and Ti, a Ky of 516 MPa×μm$^{1/2}$ was adopted here. From the EBSD results (Fig. 3-5), the average grain size in the BM zone is in the range of 1.4-5.5 μm for all the three specimens, which results in a calculated contribution from grain boundary strengthening in the range 220-436 MPa. The equivalent diameter grain size of the columnar grains in the weld joint is in the range 17.7-24 μm for all the three specimens, which results in a calculated contribution from grain boundary strengthening of 105-123 MPa. Therefore, the grain boundary strengthening contribution to the yield strength in the weld joint is clearly lower than that in the BM zone.

Fig. 6 and Fig. 7 show the high volume fraction of the $L1_2$ nanoparticles in the weld joint zone. The high volume fraction of $L1_2$ nanoparticles in the weld joints in W2 and W3 specimens led to higher hardness (Fig. 8), tensile strength, WHR (Fig. 9), and nanohardness (Fig. 10). This is due to the obstruction of dislocation movement from the precipitates. The strengthening effects of precipitates can be split into dislocation cutting through the precipitate and dislocation bypassing and looping around the precipitate [11, 54]. The precipitate shearing stress (σ_{sh}) associated with a dislocation cutting through a precipitate and Orowan dislocation looping stress (σ_{Or}) can be expressed as:

$$\sigma_{sh} = 0.81 \times M \times \frac{\gamma_{APB}}{2b} \times \left(\frac{3\pi f}{8}\right)^{1/2} \quad (6)$$

$$\sigma_{Or} = \frac{Gb}{2\pi l} \times ln\left(\frac{l}{r_0}\right) \quad (7)$$

in which M is the Taylor factor (3.06), γ_{APB} is the antiphase boundary (APB) energy of the $L1_2$ phase (184 mJ/m^2, [11, 55]), and $b = \sqrt{2}a/2$ is the Burgers vector, f is the volume fraction of $L1_2$ phase (0.29-0.33), G is the shear modulus (78.5 GPa, [11]), l is the average distance between particles, r_0 is the dislocation core radius ($r_0 \approx b$). From the TEM observations shown in Fig. 9a, the Burgers vector (b) was calculated to be around 0.248 nm. Previously, Leskovšek and Podgornik [56] used an empirical equation to calculate the mean distance l between carbide particles in high-speed steels. We used this empirical equation to calculate the mean distance l between the $L1_2$ particles, as follows:

$$l = d \times (1 - f) \times \sqrt{\frac{2}{3 \cdot f}} \tag{8}$$

For the W2 specimen, the precipitate shearing stress (σ_{sh}) and Orowan dislocation looping stress (σ_{Or}) are calculated to be 537 MPa and 805 MPa. While for the W3 specimen, the precipitate shearing stress (σ_{sh}) and Orowan dislocation looping stress (σ_{Or}) are calculated to be 573 MPa and 786 MPa. The critical size of $L1_2$ nanoparticles for the change from dislocation cutting to dislocation looping was calculated to be 28.5 nm for $Ni_{28}Co_{28}Fe_{21}Cr_{15}Al_4Ti_4$ [54] and 37 nm for $Al_{0.2}Co_{1.5}CrFeNi_{1.5}Ti_{0.3}$ [11]. Therefore, dislocation cutting through precipitated $L1_2$ nanoparticles is expected to be the predominant mechanism during plastic deformation. The contribution from $L1_2$ nanoparticles to the yield strength of the W2 and W3 specimens is very similar, with a value of 537.4 MPa and 573.3 MPa, respectively. Both are far higher than the grain boundary strengthening contribution of 105-123 MPa to the yield strength. Thus, the contribution from the lattice friction and solid solution strengthening is calculated to be around 348-441 MPa, which is a slightly higher than the range of 200-300 MPa reported previously [20, 57].

HEAs and MEAs consist of several constituent elements with different atomic sizes and electronic structures, so that their crystal lattice is expected to be distorted [58, 59]. When dislocations move through a crystal lattice under applied stresses, they interact with various crystalline defects and the attendant intrinsic lattice resistance to dislocation glide in HEAs enhances the mechanical properties [60]. Zhao et al. summarized the correlation between the lattice friction stress and the lattice distortion for various f.c.c. HEAs and MEAs [58], i.e. the lattice friction stress increases with increasing lattice distortion. In addition to lattice friction strengthening, solid solution strengthening also contributes significantly to the yield strength of the alloys. The relative contribution of the solid solution strengthening is about 50% of the yield strength in AlxCoCrCuFeNi alloys [61]. The solid-solution strengthening is based on the interaction of dislocations with solute atoms. This interaction is primarily determined by the atomic size misfit as well as the elastic modulus misfit [62, 63].

5. Conclusion

The weldability of the MEA $(NiCoCr)_{94}Al_3Ti_3$ has been explored using electron beam welding (EBW), and the effects of heat treatment on microstructure and mechanical properties of EBW MEAs have been studied. The following conclusions were reached:

(1) The EBW joint is composed of supersaturated f.c.c. matrix, showing coarse, asymmetric columnar grains with an average equivalent diameter of 17.7-24 μm and an average length-width ratio of 2.2-2.9. In addition, the twin and Σ3 CSL boundaries fraction in the weld joint is 10% of the value in the base metal zone, which increased to 30% after an aging treatment.

(2) After EBW, the Vicker hardness of the weld joint is lower than that of the base metal due to the supersaturated microstructure. The aging treatment following EBW introduces a high volume fraction (0.29-0.33) of spherical nanosized $L1_2$ particles (15.0-17.4 nm,) in the weld joint, which results in an increase in hardness, tensile strength, and work hardening rate.

(3) The contribution from $L1_2$ nanoparticles to yield strength is 537-573 MPa, which is higher than the grain boundary strengthening contribution of 105-123 MPa.

(4) The EBW MEAs show excellent weldability and good strength and ductility, with a yield strength of 1098±25 MPa, an ultimate strength of 1368±19 MPa, a fracture strain of 11±0.4%. Fracture occurs at the location of the weld joint and dimples on the fracture surface suggest a ductile fracture mechanism.

Declaration of Competing Interest

The authors declare that they have no known competing financial interests or personal relationships that could have appeared to influence the work reported in this paper.

Acknowledgments

The authors acknowledge financial support from Guangdong Provincial Department of Science and Technology (No. 2017B090907015, 2018B090904004, 2017B030314048), Guangzhou Municipal Science and Technology Bureau (No. 201907010010), and Ministry of Science and Technology of the People's Republic of China (No. 2020YFE0205300). IB was supported by the U.S. Department of Energy, Office of Science, Basic Energy Sciences, under award # DE-SC0018962.

References

[1] B. Gludovatz, A. Hohenwarter, D. Catoor, E.H. Chang, E.P. George, R.O. Ritchie, A fracture-resistant high-entropy alloy for cryogenic applications, Science 345(6201) (2014) 1153-1158.

[2] T. Yang, Y.L. Zhao, Y. Tong, Z.B. Jiao, J. Wei, J.X. Cai, X.D. Han, D. Chen, A. Hu, J.J.Kai, K. Lu, Y. Liu, C.T. Liu, Multicomponent intermetallic nanoparticles and superb mechanical behaviors of complex alloys, Science 362 (2018) 933-937.

[3] Y.J. Liang, L. Wang, Y. Wen, B. Cheng, Q. Wu, T. Cao, Q. Xiao, Y. Xue, G. Sha, Y. Wang, Y. Ren, X. Li, L. Wang, F. Wang, H. Cai, High-content ductile coherent nanoprecipitates achieve ultrastrong high-entropy alloys, Nat. Commun. 9(1) (2018) 4063.

[4] K. Yamanaka, H. Shiratori, M. Mori, K. Omura, T. Fujieda, K. Kuwabara, A. Chiba, Corrosion mechanism of an equimolar AlCoCrFeNi high-entropy alloy additively manufactured by electron beam melting, npj Mater. Degrad. 4(1) (2020).

[5] K. Kuwabara, H. Shiratori, T. Fujieda, K. Yamanaka, Y. Koizumi, A. Chiba, Mechanical and corrosion properties of AlCoCrFeNi high-entropy alloy fabricated with selective electron beam melting, Addit. Manuf. 23 (2018) 264-271.

[6] N.A.P.K. Kumar, C. Li, K.J. Leonard, H. Bei, S.J. Zinkle, Microstructural stability and mechanical behavior of FeNiMnCr high entropy alloy under ion irradiation, Acta Mater. 113 (2016) 230-244.

[7] Y.P. Lin, T.F. Yang, L. Lang, C. Shan, H.Q. Deng, W.Y. Hu, F. Gao, Enhanced radiation tolerance of the Ni-Co-Cr-Fe high-entropy alloy as revealed from primary damage, Acta Mater. 196 (2020) 133-143.

[8] J. Yang, J.W. Qiao, S.G. Ma, G.Y. Wu, D. Zhao, Z.H. Wang, Revealing the Hall-Petch relationship of Al0.1CoCrFeNi high-entropy alloy and its deformation mechanisms, J. Alloys Compd. 795 (2019) 269-274.

[9] N.D. Stepanov, D.G. Shaysultanov, R.S. Chernichenko, D.M. Ikornikov, V.N. Sanin, S.V. Zherebtsov, Mechanical properties of a new high entropy alloy with a duplex ultra-fine grained structure, Mater. Sci. Eng. A 728 (2018) 54-62.

[10] T. Yang, Y.L. Zhao, W.H. Liu, J.J. Kai, C. Liu, $L1_2$-strengthened high-entropy alloys for advanced structural applications, J. Mater. Res. 33(19) (2018) 2983-2997.

[11] K.S. Ming, X.F. Bi, J. Wang, Realizing strength-ductility combination of coarse-grained Al0.2Co1.5CrFeNi1.5Ti0.3 alloy via nano-sized, coherent precipitates, Int. J. Plast. 100 (2018) 177-191.

[12] S.R. Reddy, S. Yoshida, U. Sunkari, A. Lozinko, J. Joseph, R. Saha, D. Fabijanic, S. Guo, P.P. Bhattacharjee, N. Tsuji, Engineering heterogeneous microstructure by severe warm-rolling for enhancing strength-ductility synergy in eutectic high entropy alloys, Mater. Sci. Eng. A 764 (2019) 138226.

[13] X.H. Du, W.P.Li, H.T. Chang, T. Yang, G.S. Duan, B.L.Wu, J.C. Huang, F.R. Chen, C.T. Liu, W.S. Chuang, Y. Lu, M.L. Sui, E.W. Huang, Dual heterogeneous structures lead to ultrahigh strength and uniform ductility in a Co-Cr-Ni medium-entropy alloy, Nat. Commun. 11 (2020) 2390

[14] I. Baker, Interstitials in f.c.c. high entropy alloys, Metals 10(5) (2020) 695-715.

[15] N.D. Stepanov, N.Y. Yurchenko, M.A. Tikhonovsky, G.A. Salishchev, Effect of carbon content and annealing on structure and hardness of the CoCrFeNiMn-based high entropy alloys, J. Alloys Compd. 687 (2016) 59-71.

[16] Z.W. Wang, I. Baker, Interstitial strengthening of a f.c.c. FeNiMnAlCr high entropy alloy, Mater. Lett. 180 (2016) 153-156.

[17] S. Jiang, H. Wang, Y. Wu, X. Liu, H. Chen, M. Yao, B. Gault, D. Ponge, D. Raabe, A. Hirata, M. Chen, Y. Wang, Z. Lu, Ultrastrong steel via minimal lattice misfit and high-density nanoprecipitation, Nature 544(7651) (2017) 460-464.

[18] R.P. Zhang, S.T. Zhao, J. Ding, Y. Chong, T. Jia, C. Ophus, M. Asta, R.O. Ritchie, A.M. Minor, Short-range order and its impact on the CrCoNi medium-entropy alloy, Nature 581(7808) (2020) 283-287.

[19] Y. Tong, D. Chen, B. Han, Wang, R. Feng, T. Yang, C. Zhao, Y.L. Zhao, W. Guo, Y. Shimizu, C.T. Liu, P.K. Liaw, K. Inoue, Y. Nagai, A. Hu, Kai, Outstanding tensile properties of a precipitation-strengthened FeCoNiCrTi0.2 high-entropy alloy at room and cryogenic temperatures, Acta Mater. 165 (2019) 228- 240.

[20] H.L. Peng, L. Hu, L.J. Li, J.X. Gao, Q. Zhang, On the correlation between L12 nanoparticles and mechanical properties of $(NiCo)_{52+2x}(AlTi)_{4+2x}Fe_{29-4x}Cr_{15}$ (x=0-4) high-entropy alloys, J. Alloys Compd. 817 (2020) 152750.

[21] B.X. Cao, H.J. Kong, Z.Y. Ding, S.W. Wu, J.H. Luan, Z.B. Jiao, J. Lu, C.T. Liu, T. Yang, A novel L12-strengthened multicomponent Co-rich high-entropy alloy with both high γ-solvus temperature and superior high-temperature strength, Scr. Mater. 199 (2021) 113826.

[22] H. Daoud, A.M. Manzoni, N. Wanderka, High-temperature tensile strength of Al10Co25Cr8Fe15Ni36Ti6 compositionally complex alloy (high-entropy alloy), JOM 67(10) (2015) 2271-2277.

[23] T. Yang, Y.L. Zhao, L. Fan, J. Wei, J.H. Luan, W.H. Liu, C. Wang, Z.B. Jiao, J.J. Kai, C.T. Liu, Control of nanoscale precipitation and elimination of intermediate-temperature embrittlement in multicomponent high-entropy alloys, Acta Mater. 189 (2020) 47-59.

[24] T. Yang, Y.L. Zhao, W.P. Li, C.Y. Yu, J.H. Luan, D.Y. Lin, L.Fan, Z.B. Jiao, W.H. Liu, X.J. Liu, J.J. Kai, J.C. Huang, C.T. Liu, Ultrahigh-strength and ductile superlattice alloys with nanoscale disordered interfaces, Science 369 (2020) 427–432

[25] H.L. Peng, I. Baker, L. Hu, L.J. Li, Superior strength-ductility synergy in a novel tailored nanoparticles-strengthened medium-entropy alloy, Scr. Mater. 207 (2022) 114278.

[26] N. Kashaev, V. Ventzke, N. Petrov, M. Horstmann, S. Zherebtsov, D. Shaysultanov, V. Sanin, N. Stepanov, Fatigue behaviour of a laser beam welded CoCrFeNiMn-type high entropy alloy, Mater. Sci. Eng. A 766 (2019) 138358.

[27] N. Kashaev, V. Ventzke, N. Stepanov, D. Shaysultanov, V. Sanin, S. Zherebtsov, Laser beam welding of a CoCrFeNiMn-type high entropy alloy produced by self-propagating high-temperature synthesis, Intermetallics 96 (2018) 63-71.

[28] H. Nam, S. Park, E.J. Chun, H. Kim, Y. Na, N. Kang, Laser dissimilar weldability of cast and rolled CoCrFeMnNi high-entropy alloys for cryogenic applications, Sci. Technol. Weld. Joining 25(2) (2019) 127-134.

[29] H. Nam, C. Park, J. Moon, Y. Na, H. Kim, N. Kang, Laser weldability of cast and rolled high-entropy alloys for cryogenic applications, Mater. Sci. Eng. A 742 (2019) 224-230.

[30] Z. Wu, S.A. David, Z. Feng, H. Bei, Weldability of a high entropy CrMnFeCoNi alloy, Scr. Mater. 124 (2016) 81-85.

[31] J.P. Oliveira, J.J. Shen, Z. Zeng, J.M. Park, Y.T. Choi, N. Schell, E. Maawad, N. Zhou, H.S. Kim, Dissimilar laser welding of a CoCrFeMnNi high entropy alloy to 316 stainless steel, Scr. Mater. 206 (2022) 114219.

[32] R. Sokkalingam, P. Mastanaiah, V. Muthupandi, K. Sivaprasad, K.G. Prashanth, Electron-beam welding of high-entropy alloy and stainless steel: microstructure and mechanical properties, Mater. Manuf. Processes 35(16) (2020) 1885-1894.

[33] A. Mashhuriazar, H. Omidvar, C.H. Gur, Z. Sajuri, Effect of Welding Parameters on the Liquation Cracking Behavior of High-Chromium Ni-Based Superalloy, *J. Mater. Eng. Perform.* 29(12) (2020) 7843-7852.

[34] J.J. Xu, X. Lin, Y.F. Zhao, P.F. Guo, X.L. Wen, Q.G. Li, H.O. Yang, H.B. Dong, L. Xue, W.D. Huang, HAZ Liquation Cracking Mechanism of IN-738LC Superalloy Prepared by Laser Solid Forming, Metall. Mater. Trans. A 49(10) (2018) 5118-5136.

[35] M. Rhode, T. Richter, D. Schroepfer, A.M. Manzoni, M. Schneider, G. Laplanche, Welding of high-entropy alloys and compositionally complex alloys—an overview, Weld. World 65(8) (2021) 1645-1659.

[36] Z.W. Zhu, X.Q. Ma, C.M. Wang, G.Y. Mi, Altering morphological, crystalline and compositional features in 316 L laser-MIG weldments with an external magnetic field, Mater. Des. 196 (2020) 109156.

[37] M. Calcagnotto, D. Ponge, E. Demir, D. Raabe, Orientation gradients and geometrically necessary dislocations in ultrafine

grained dual-phase steels studied by 2D and 3D EBSD, Mater. Sci. Eng. A 527(10-11) (2010) 2738-2746.

[38] X.L. Shen, K. Gao, S.J. Dong, Simulation and analysis of electron beam welding residual stress in thin-walled high-temperature alloy aeroengine structures, Int. J. Adv. Manuf. Technol. 107(9-10) (2020) 3953-3966.

[39] X.L. Huang, L.P. Huang, H.L. Peng, Y. Liu, B. Liu, S. Li, Enhancing strength-ductility synergy in a casting non-equiatomic NiCoCr-based high-entropy alloy by Al and Ti combination addition, Scr. Mater. 200(113898) (2021).

[40] J.Y. He, W.H. Liu, H. Wang, Y. Wu, X.J. Liu, T.G. Nieh, Z.P. Lu, Effects of Al addition on structural evolution and tensile properties of the FeCoNiCrMn high-entropy alloy system, Acta Mater. 62 (2014) 105-113.

[41] S.G. Ma, S.F. Zhang, J.W. Qiao, Z.H. Wang, M.C. Gao, Z.M. Jiao, H.J. Yang, Y. Zhang, Superior high tensile elongation of a single-crystal CoCrFeNiAl0.3 high-entropy alloy by Bridgman solidification, Intermetallics 54 (2014) 104-109.

[42] Z.Z. Niu, Y. Xie, E. Axinte, J. Xu, Y. Wang, Development and characterization of novel Ni-rich high-entropy alloys, J. Alloys Compd. 846 (2020) 156342.

[43] L. Jiang, Y.P. Lu, M. Song, C. Lu, K. Sun, Z.Q. Cao, T.M. Wang, F. Gao, L.M. Wang, A promising CoFeNi2V0.5Mo0.2 high entropy alloy with exceptional ductility, Scr. Mater. 165 (2019) 128-133.

[44] R. Ding, Z.B. Dai, M.X. Huang, Z.G. Yang, C. Zhang, H. Chen, Effect of pre-existed austenite on austenite reversion and mechanical behavior of an Fe-0.2C-8Mn-2Al medium Mn steel, Acta Mater. 147 (2018) 59-69.

[45] L. Hu, H.L. Peng, I. Baker, L.J. Li, W.P. Zhang, T. Ngai, Characterization of high-strength high-nitrogen austenitic stainless steel synthesized from nitrided powders by spark plasma sintering, Mater. Charact. 152 (2019) 76-84.

[46] R. Song, D. Ponge, D. Raabe, Improvement of the work hardening rate of ultrafine grained steels through second phase particles, Scr. Mater. 52(11) (2005) 1075-1080.

[47] Z.W. Wang, A. Genc, I. Baker, Direct versus indirect particle strengthening in a strong, ductile FeNiMnAlTi high entropy alloy, Mater. Charact. 132 (2017) 156-161.

[48] Z.W. Wang, I. Baker, W. Guo, J.D. Poplawsky, The effect of carbon on the microstructures, mechanical properties, and deformation mechanisms of thermo-mechanically treated $Fe_{40.4}Ni_{11.3}Mn_{34.8}Al_{7.5}Cr_6$ high entropy alloys, Acta Mater. 126 (2017) 346-360.

[49] B.B. He, Z.Y. Liang, M.X. Huang, Nanoindentation investigation on the initiation of yield point phenomenon in a medium Mn steel, Scr. Mater. 150 (2018) 134-138.

[50] B.B. He, M.X. Huang, Z.Y. Liang, A.H.W. Ngan, H.W. Luo, J. Shi, W.Q. Cao, H. Dong, Nanoindentation investigation on the mechanical stability of individual austenite grains in a medium-Mn transformation-induced plasticity steel, Scr. Mater. 69(3) (2013) 215-218.

[51] A. Haglund, M. Koehler, D. Catoor, E.P. George, V. Keppens, Polycrystalline elastic moduli of a high-entropy alloy at cryogenic temperatures, Intermetallics 58 (2015) 62-64.

[52] S. Yoshida, T. Bhattacharjee, Y. Bai, N. Tsuji, Friction stress and Hall-Petch relationship in CoCrNi equi-atomic medium entropy alloy processed by severe plastic deformation and subsequent annealing, Scr. Mater. 134 (2017) 33–36.

[53] L. Fan, T. Yang, Y. Zhao, J. Luan, G. Zhou, H. Wang, Z.B. Jiao, C.T. Liu, Ultrahigh strength and ductility in newly developed materials with coherent nanolamellar architectures, Nat. Commun. 11(1) (2020) 6240.

[54] H.L. Peng, L. Hu, L.J. Li, W.P. Zhang, Ripening of $L1_2$ nanoparticles and their effects on mechanical properties of $Ni_{28}Co_{28}Fe_{21}Cr_{15}Al_4Ti_4$ high-entropy alloys, Mater. Sci. Eng. A 772 (2020) 138803.

[55] T. Kruml, E. Conforto, B.L. Piccolo, D. Caillard, J.L. Martin, From dislocation cores to strength and work-hardening: a study of binary Ni3Al, Acta Mater. 50 (2002) 5091–5101.

[56] V. Leskovšek, B. Podgornik, Vacuum heat treatment, deep cryogenic treatment and simultaneous pulse plasma nitriding and tempering of P/M S390MC steel, Mater. Sci. Eng. A 531 (2012) 119-129.

[57] Z. Wu, H. Bei, G.M. Pharr, E.P. George, Temperature dependence of the mechanical properties of equiatomic solid solution alloys with face-centered cubic crystal structures, Acta Mater. 81 (2014) 428–441.

[58] Y.Y. Zhao, T.G. Nieh, Correlation between lattice distortion and friction stress in Ni-based equiatomic alloys, Intermetallics 86 (2017) 45-50.

[59] J. Moon, M.J. Jang, J.W. Bae, D. Yim, J.M. Park, J. Lee, H.S. Kim, Mechanical behavior and solid solution strengthening

model for face-centered cubic single crystalline and polycrystalline high-entropy alloys, Intermetallics 98 (2018) 89-94.
[60] Z. Wu, Y.F. Gao, H. Bei, Single crystal plastic behavior of a single-phase, face-center-cubic-structured, equiatomic FeNiCrCo alloy, Scr. Mater. 109 (2015) 108-112.
[61] R. Sriharitha, B.S. Murty, R.S. Kottada, Alloying, thermal stability and strengthening in spark plasma sintered AlxCoCrCuFeNi high entropy alloys, J. Alloys Compd. 583 (2014) 419-426.
[62] M. Lugovy, V. Slyunyayev, M. Brodnikovskyy, WITHDRAWN: Solid solution strengthening in multiprincipal element fcc and bcc alloys: analytical approach, Progress in Natural Science: Materials International (2020).
[63] J.Y. He, H. Wang, H.L. Huang, X.D. Xu, M.W. Chen, Y. Wu, X.J. Liu, T.G. Nieh, K. An, Z.P. Lu, A precipitation-hardened high-entropy alloy with outstanding tensile properties, Acta Mater. 102 (2016) 187-196.